Radiation-Field Transformation, Particle Transport, and High-LET Attenuation in Aluminum Shielding on The Martian Surface Using NASA OLTARIS/HZETRN

Abba, A. M.[1] and Ahmad, I.[2]*
Department of Physics,
Bayero University, Kano, Nigeria
Email: iahmad.phy@buk.edu.ng: amabba32@gmail.com
https://doi.org/10.56201/rjpst.vol.9.no8.2026.pg57.68

Abstract
Galactic Cosmic Rays (GCRs) pose a persistent radiation hazard for long-duration human exploration beyond Earth's magnetosphere. This study characterizes the transformation of the Martian-surface GCR radiation field as it traverses increasing aluminum areal density using NASA's Online Tool for the Assessment of Radiation in Space (OLTARIS) and its HZETRN transport framework. The recorded simulation employed the Badhwar–O'Neill 2020 (BO-20) GCR model, 2010 solar-minimum conditions, a 687-day mission duration, spherical aluminum shielding, and eleven areal-density cases from 0 to 100 g cm^{-2}. Energy-integrated particle flux, species-resolved transport, particle-resolved absorbed-dose fractions, and differential and integral Linear Energy Transfer (LET) were evaluated. Total transported particle flux increased from approximately 491.3 to 1477.6 particles cm^{-2} day^{-1} between 0 and 100 g cm^{-2}, whereas Ni-58 flux decreased by 99.88% and proton flux increased by 372.6%. The heavy-ion contribution to absorbed dose decreased from 96.65% to 8.20%, while proton, electron/positron, pion, and D/T/He contributions became more prominent. Cumulative flux above 10, 100, and 1000 keV μm^{-1} decreased by approximately 88.05%, 99.07%, and 99.59%, respectively. These results demonstrate that aluminum shielding transforms the radiation field through nuclear fragmentation and secondary-particle production rather than simply reducing particle number. Because the recorded OLTARIS configuration includes a nickel-specific selection, the particle-resolved dose fractions are configuration-specific and should not be interpreted as the natural GCR elemental composition. The resulting dataset provides a traceable aluminum transport baseline for subsequent evaluation of hydrogen-rich, regolith, and hybrid shielding systems.

Keywords: *Galactic Cosmic Rays; Martian Surface; Aluminum Shielding; OLTARIS; HZETRN; Secondary Radiation; Particle Transport; LET; HZE Ions; Radiation Quality*

1. Introduction

Radiation protection for human Mars missions requires more than determining how much incident radiation is removed by a shielding wall. Galactic Cosmic Rays are a mixed field containing protons, helium nuclei, and heavier ions extending to high atomic number and high kinetic energy. The Martian atmosphere attenuates part of the incident field, but the surface remains exposed to a persistent radiation environment. Measurements by the Mars Science Laboratory's Radiation Assessment Detector established the importance of the surface radiation field and provide an observational basis for computational transport studies [1].

The interaction of GCRs with shielding is governed by coupled electromagnetic and nuclear processes. Charged particles lose energy, undergo nuclear reactions, and can fragment into lighter nuclei. Secondary neutrons, protons, electrons, photons, pions, and other particles may consequently be produced within the shielding. A thicker shield can therefore reduce the abundance of an incident heavy ion while increasing the number of secondary particles. Total particle flux is consequently not, by itself, a monotonic measure of shielding performance.

This distinction is particularly important for high-LET radiation. Heavy ions can deposit energy densely along their tracks and may contribute strongly to biological damage even when their numerical abundance is relatively small. Radiation-quality metrics such as LET, dose equivalent, and biological response functions are therefore complementary to conventional particle-flux analysis [2,3]. Aluminum is an established aerospace structural material and provides a useful reference material for radiation-shielding studies. Its engineering utility is accompanied by the possibility of nuclear fragmentation and secondary-particle production, making the material useful for examining the difference between simple attenuation and radiation-field transformation. Previous HZETRN/OLTARIS investigations have shown that shielding performance depends on the balance among attenuation, secondary production, and material mass [4–7]. The present study focuses specifically on the transported radiation field behind increasing aluminum areal density. The objectives are to quantify energy-integrated particle flux, compare proton and Ni-58 transport, determine how particle contributions to absorbed dose are redistributed, quantify suppression of high-LET components, and establish transport-based indicators suitable for subsequent comparison of alternative shielding materials.

An important interpretive constraint applies throughout the analysis. The recorded OLTARIS configuration identifies nickel (Z = 28) as the selected specific ion. Accordingly, the large heavy-ion and Ni-58 dose fractions reported here describe the recorded computational response configuration and must not be interpreted as the natural elemental abundance of heavy ions in the incident GCR population. The Martian boundary spectrum itself contains the light-ion populations expected in GCRs.

2. Materials and Methods

2.1 OLTARIS/HZETRN Configuration

Table 1. OLTARIS configuration and principal multidimensional output grids.

Parameter	Recorded setting
Radiation environment	Galactic Cosmic Rays
Planetary environment	Martian surface
GCR model	Badhwar–O'Neill 2020
Solar condition	2010 solar minimum
Mission duration	687 days
Shield geometry	Sphere
Shield material	Aluminum; 2.7 g cm^{-3}
Selected ion	Nickel; Z = 28
Aluminum areal densities	0, 0.1, 0.3, 0.5, 1, 3, 5, 10, 30, 50, 100 g cm^{-2}
Flux grid	125 energy points × 66 particle categories × 11 Al depths × 11 tissue depths
LET grid	1,000 LET points × 11 Al depths × 11 tissue depths

The transport balance used to describe the HZETRN calculation may be written in the following standard loss-plus-production form:

$[\partial/\partial x - (1/A_j)\partial/\partial E\ S_j(E) + \sigma_j(E)]\varphi_j(x,E) = \Sigma_k \int_E^\infty \sigma_{k\to j}(E,E')\varphi_k(x,E')\ dE'$ ……………….. (1)

Here, φ_j is the differential fluence/flux of particle type j, x is transport depth, E is kinetic energy per nucleon, A_j is the particle atomic mass, $S_j(E)$ is the stopping-power term, $\sigma_j(E)$ is the total macroscopic removal cross section, and $\sigma_{k\to j}$ represents production of type j from an incident type k population. The equation makes explicit that the transmitted field is determined jointly by losses from incident populations and gains from secondary production.

2.2 Raw OLTARIS Data Products

Table 2. OLTARIS output files used for transport and radiation-quality analysis.

Raw output	Use in the present study
hi_flux_database.dat	Energy-resolved transported flux for 66 particle categories, 11 aluminum cases, and 11 tissue-depth points
hi_Flux_Point_1.dat	Energy-resolved flux at Point 1
hi_mars_surface_bc.dat	Martian-surface isotropic boundary spectrum
hi_dose_frac_database.dat	Particle fraction of absorbed dose
hi_dose_part_database_mGy.dat	Particle-specific absorbed dose
hi_diflet_table.dat	Differential LET versus aluminum and tissue depth
hi_intlet_table.dat	Integral LET versus aluminum and tissue depth
hi_doseq_NASA_Leukemia_frac_database.dat	Particle fractions of leukemia response
hi_doseq_NASA_Solid_Cancer_frac_database.dat	Particle fractions of solid-cancer response

2.3 Energy-Integrated Particle Flux

The differential particle flux, $\Phi_j(E,x)$, was integrated over the exported OLTARIS energy grid to obtain an energy-integrated particle flux for each particle species and aluminum areal density:

$F_j(x) = \int \Phi_j(E,x)\ dE$ ……………………………………………………………. (2)

Numerical integration was performed using the trapezoidal rule over the exported energy grid. Photon, electron, and positron channels use energy in MeV, whereas the other particle categories use MeV/amu; integration was therefore performed separately within each particle category before summation. The resulting total is a transport-field metric and is not a dosimetric quantity.

2.4 LET Analysis

The differential LET output provides flux density as a function of LET, while the integral LET output represents cumulative flux above a given LET coordinate. The cumulative fraction above a threshold L was evaluated as:

$f_{(>L)} = [F_{(>L)} / F_{(>0.1\ keV\ \mu m^{-1})}] \times 100$ ………………………………….. (3)

Thresholds of 1, 10, 100, and 1000 keV μm^{-1} were selected to characterize progressively higher-LET portions of the spectrum. The integral LET output was used directly, avoiding interpolation between non-tabulated thresholds.

2.5 Particle-Group Classification

For interpretation, the 66 OLTARIS particle categories were grouped into photons; electrons/positrons; muons; pions; neutrons; protons; deuterons, tritons and helium nuclei (D/T/He); and heavy ions from Li through Ni. Group fractions were calculated from the normalized absorbed-dose fraction database at zero tissue depth. This preserves the distinction between particle abundance and deposited energy and avoids treating a particle count as a surrogate for dose.

2.6 Data Quality and Internal Closure

The dose-fraction array was reconstructed using its explicit dimensions of 11 aluminum cases × 11 tissue-depth cases × 66 particle categories. At zero tissue depth, the 66 fractions sum to unity within numerical round-off for every aluminum case. Particle-specific absorbed-dose channels likewise close to the corresponding total absorbed dose. During review, the apparent residual contribution in the grouped dose table was traced to the D/T/He channels rather than neutrons; the revised table below therefore reports D/T/He explicitly. This correction preserves the original raw fractions and resolves the internal inconsistency in the previous manuscript.

3. Results

3.1 Total Transported Particle Flux

The total energy-integrated transported particle flux increased from approximately 491.3 particles cm^{-2} day^{-1} without aluminum to 1477.6 particles cm^{-2} day^{-1} at 100 g cm^{-2}, corresponding to an increase by a factor of approximately 3.01. This increase occurs despite the reduction in absorbed dose reported for the same shielding sequence. The two quantities describe different properties of the transported field and should not be interpreted as equivalent measures of shielding performance.

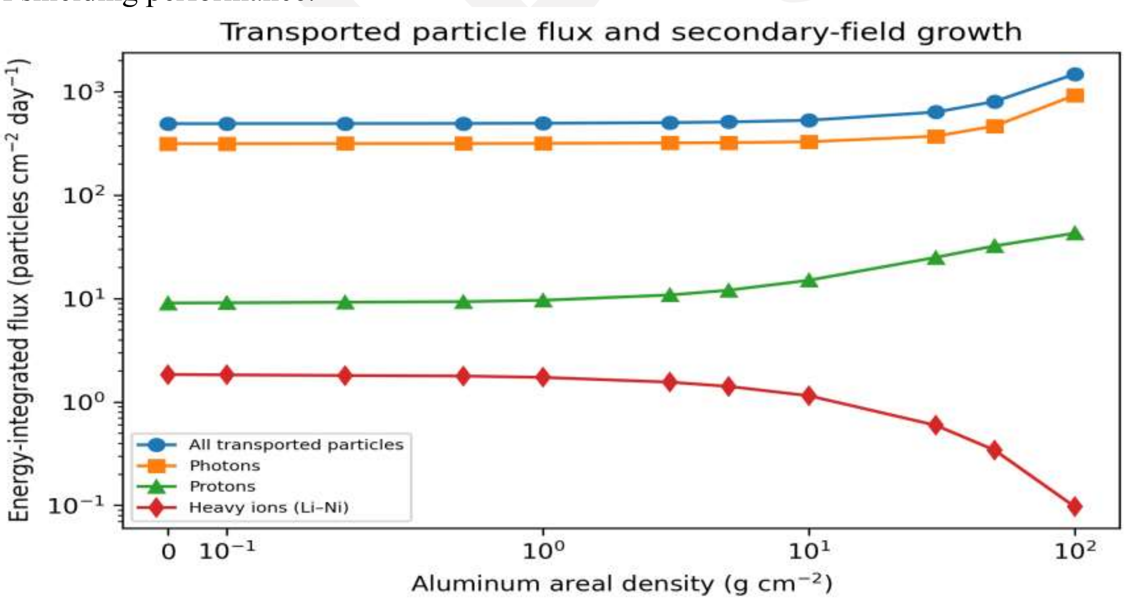

Figure 1. Energy-integrated transported particle flux and selected particle-group flux as functions of aluminum areal density.

The increase in total flux is associated with secondary-particle buildup. Photon flux rises from approximately 315.2 to 923.3 particles cm^{-2} day^{-1}, electron/positron flux from 7.52 to 64.18 particles cm^{-2} day^{-1}, and proton flux from 9.06 to 42.80 particles cm^{-2} day^{-1}. In contrast, the heavy-ion flux for the Li–Ni group decreases from approximately 1.84 to 0.097 particles cm^{-2} day^{-1}.

3.2 Proton–Ni-58 Transport Contrast

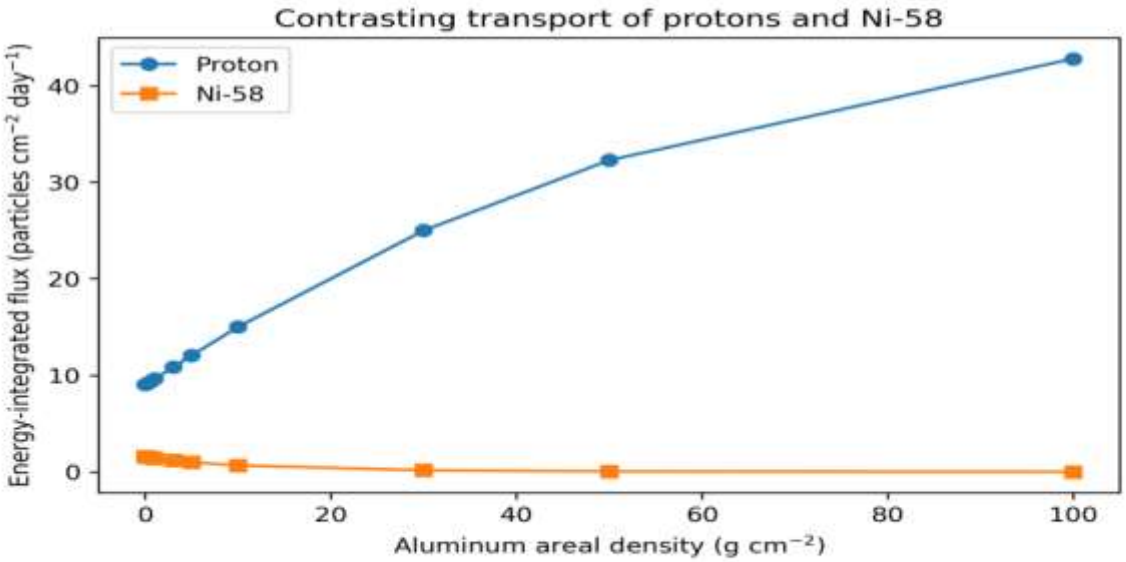

Figure 2. Energy-integrated proton and Ni-58 flux at zero tissue depth.

Proton and Ni-58 transport show opposite trends. Proton flux increases by approximately 372.6% between the unshielded condition and 100 g cm^{-2}, whereas Ni-58 flux decreases by approximately 99.88%. At 30 g cm^{-2}, the Ni-58 flux has already fallen by approximately 90.0%, while the proton flux is about 25.0 particles cm^{-2} day^{-1}. At 50 g cm^{-2}, the Ni-58 flux is approximately 0.0414 particles cm^{-2} day^{-1} compared with 32.3 particles cm^{-2} day^{-1} for protons. At 100 g cm^{-2}, the Ni-58 component is almost extinguished in the integrated transport metric, while the proton population remains substantial.

The opposing trends should not be interpreted as one-to-one conversion of heavy ions into protons. The proton channel contains surviving incident protons together with secondary protons produced through nuclear interactions. The database therefore records aggregate radiation-field transformation through multiple interaction pathways.

3.3 Absorbed-Dose Composition

Table 3. Selected particle-group contributions to absorbed dose at zero tissue depth (%). Values were reconstructed from the raw OLTARIS dose-fraction database; D/T/He is shown explicitly to resolve the residual fraction present in the original grouping.

Al (g cm^{-2})	Heavy ions Li–Ni	Protons	e±	π±	Neutrons	D/T/He	μ±	Photons
0	96.65	1.64	0.38	0.17	0.00	1.00	0.16	0.00
10	91.80	4.29	0.96	0.61	0.00	2.09	0.24	0.00
30	70.59	15.87	3.78	3.15	0.00	6.16	0.45	0.00
50	42.23	30.84	9.53	7.47	0.00	9.32	0.60	0.01
100	8.20	44.93	23.50	13.80	0.00	8.98	0.57	0.01

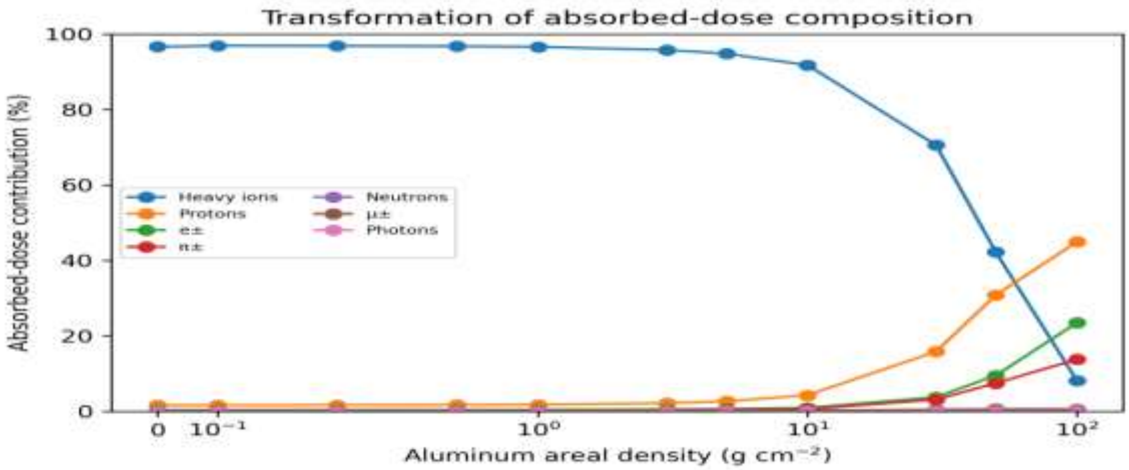

Figure 3. Transformation of absorbed-dose composition with increasing aluminum areal density.

The composition of absorbed dose changes markedly with increasing aluminum. The heavy-ion Li–Ni group decreases from 96.65% at zero aluminum to 91.80% at 10 g cm^{-2}, 70.59% at 30 g cm^{-2}, 42.23% at 50 g cm^{-2}, and 8.20% at 100 g cm^{-2}. Over the same range, the proton contribution rises from 1.64% to 44.93%, electrons/positrons from 0.38% to 23.50%, pions from 0.17% to 13.80%, and D/T/He from 1.00% to 8.98%.

Ni-58 alone contributes approximately 89.57% of the absorbed-dose fraction at zero aluminum in the recorded output. This value is a property of the selected OLTARIS response configuration and is not the natural fraction of nickel nuclei in the incident GCR population.

3.4 Cumulative High-LET Flux

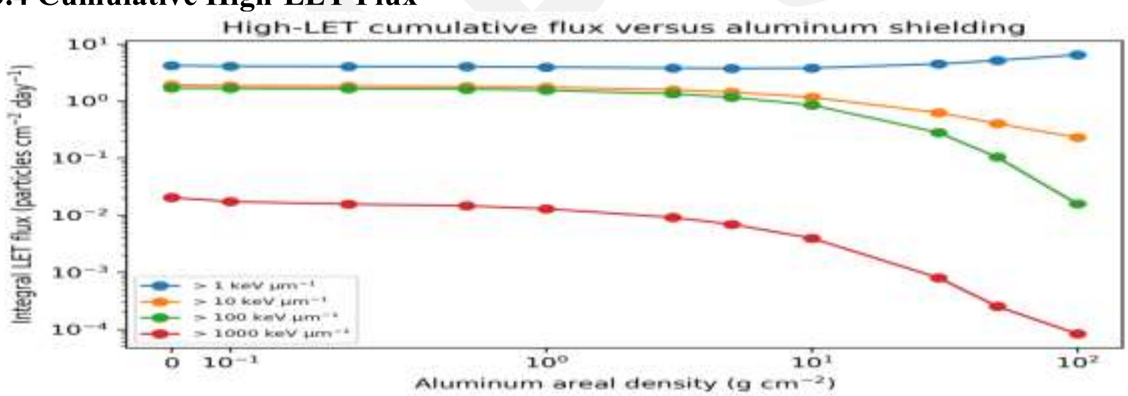

Figure 4. Integral flux above selected LET thresholds as a function of aluminum areal density.

Table 4. Cumulative LET-flux response between the unshielded and 100 g cm^{-2} aluminum cases.

LET threshold (keV μm^{-1})	0 g cm^{-2}	100 g cm^{-2}	Reduction (%)	Fraction at 0 (%)	Fraction at 100 (%)
>1	4.1889	6.43868	−53.71	16.28	4.4772
>10	1.91968	0.229309	88.05	7.46	0.1595
>100	1.69591	0.01579	99.07	6.59	0.0110
>1000	0.0203396	8.3301×10^{-5}	99.59	0.08	0.0001

The cumulative high-LET population is strongly suppressed with increasing aluminum. Flux above 10 keV μm^{-1} decreases from approximately 1.920 to 0.229 particles cm^{-2} day^{-1}, a reduction of 88.05%. Above 100 keV μm^{-1}, it decreases from approximately 1.696 to 0.0158 particles cm^{-2} day^{-1}, a reduction of 99.07%. Above 1000 keV μm^{-1}, it decreases from approximately 2.03×10^{-2} to 8.33×10^{-5} particles cm^{-2} day^{-1}, a reduction of 99.59%.
The >1 keV μm^{-1} component increases by 53.71%. This result is consistent with secondary-particle buildup at lower LET and reinforces the need to distinguish suppression of the extreme-LET tail from changes in the overall transported particle population.

3.5 Differential LET Spectrum

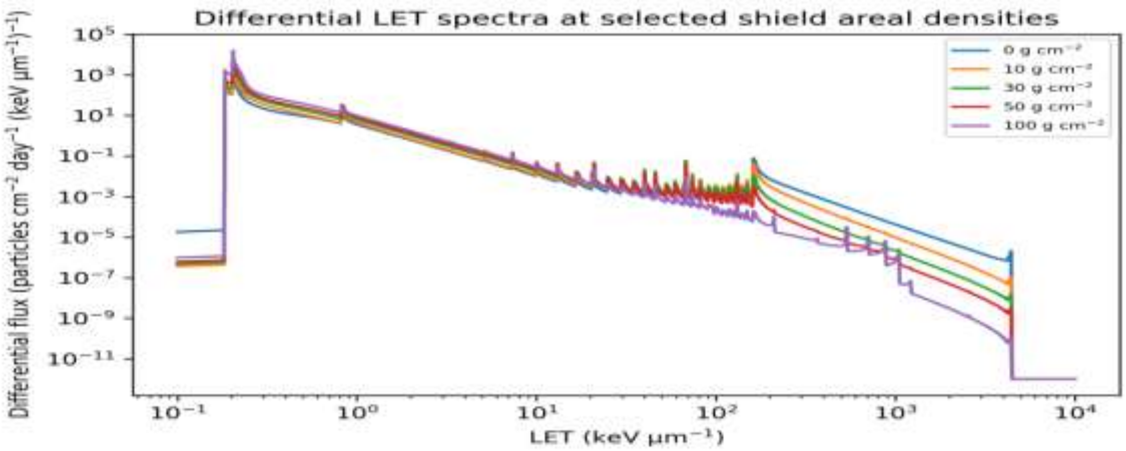

Figure 5. Differential LET spectra for selected aluminum areal densities at zero tissue depth.
The differential LET distributions span approximately 0.1 to 10,000 keV μm^{-1} over 1,000 sampling points. The spectra contain a broad low-LET population and a substantially smaller high-LET tail. As aluminum areal density increases, the extreme-LET portion is progressively reduced while lower-LET components become relatively more prominent.

3.6 Integral LET Spectrum

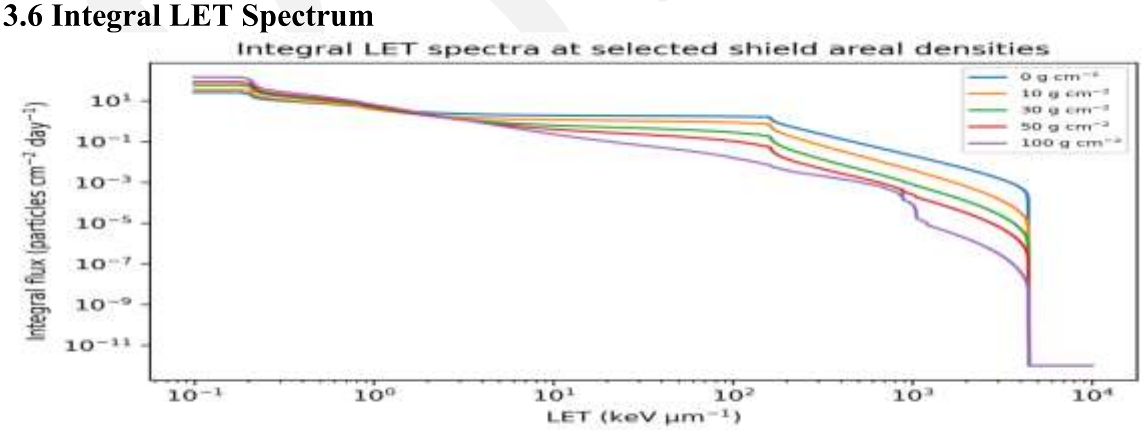

Figure 6. Integral LET spectra for selected aluminum areal densities at zero tissue depth.
The integral LET spectra provide a cumulative representation of the same transformation. Flux decreases with increasing LET, while the high-LET portion shifts downward as aluminum thickness increases. At the lowest LET range, the integral flux can increase because secondary-

particle production adds lower-LET particles. Thus, a reduction in high-LET flux can coexist with an increase in lower-LET fluence while the overall radiation response is reduced.

4. Discussion

4.1 Radiation-Field Transformation and Secondary-Particle Production

The dominant transport result is the increase in total transported particle flux with aluminum areal density. The approximately threefold increase between 0 and 100 g cm^{-2} does not represent a deterioration of shielding effectiveness in dosimetric terms. Instead, it reflects the production and transport of secondary particles generated when energetic primaries interact with aluminum.
The simultaneous decrease in Li–Ni and Ni-58 flux and increase in proton, electron/positron, pion, and photon populations provides direct evidence that the transmitted field becomes compositionally different from the incident or selected primary field. This is the characteristic behavior expected when nuclear fragmentation, particle removal, energy loss, and secondary production operate together.

4.2 Particle Flux versus Absorbed Dose

The results demonstrate why total particle count should not be used as a stand-alone shielding-performance criterion. Particle flux is sensitive to multiplicity: one energetic primary can generate several lower-energy secondaries. Absorbed dose, by contrast, depends on energy deposition, and biological response additionally depends on radiation quality. The observed increase in particle flux alongside suppression of the high-LET tail therefore represents a redistribution of radiation rather than a simple increase or decrease in risk.
This distinction also explains why the transport results complement the dose-focused findings of the broader shielding analysis without duplicating them. The present paper identifies how the radiation field changes internally, whereas a shielding assessment based only on total dose would not reveal that redistribution.

4.3 Transformation of Radiation Quality

The strong reduction in cumulative flux above 10, 100, and 1000 keV μm^{-1} indicates preferential suppression of the extreme-LET tail. At the same time, the lower-LET population becomes relatively more prominent as secondary particles accumulate. The differential and integral LET spectra show that aluminum modifies both the magnitude and the shape of the transmitted radiation-quality distribution.
The heavy-ion contribution to absorbed dose falls from 96.65% to 8.20% in the recorded specific-ion configuration, while protons and other secondary groups become more important. This is consistent with progressive attenuation and fragmentation of high-Z primaries. However, the nickel-specific configuration limits the extent to which these fractions can be generalized to the full GCR elemental population.

4.4 Implications for Space-Radiation Protection

The findings support a multidimensional approach to shielding optimization. Total transported particle flux alone can be misleading because it may rise as shielding becomes thicker. Conversely, absorbed dose alone can obscure the persistence of biologically important radiation-quality components. A robust assessment should therefore consider, at minimum, absorbed dose, biologically weighted dose where available, species-resolved flux, and LET distributions.

For aluminum, increasing areal density strongly suppresses the original high-Z component and extreme-LET tail but progressively produces a transmitted field richer in secondary particles. This behavior supports the use of aluminum as a structural reference material while motivating comparison with hydrogen-rich, polymeric, regolith, and hybrid shielding systems.

4.5 Comparison with Previous Studies

Previous HZETRN/OLTARIS studies have shown that aluminum and polyethylene do not behave identically under GCR transport and that high-energy heavy ions remain important components of the residual field [4,8]. The present analysis adds a transport-field perspective by explicitly demonstrating that total integrated particle flux can increase while heavy-ion and high-LET components decrease. Studies of hydrogen-rich materials and metal hydrides have reported different dose-equivalent responses from aluminum under selected GCR configurations and have emphasized the importance of material ordering in multilayer shields [8]. The present aluminum results therefore provide a complementary baseline: future material comparisons should evaluate not only dose reduction but also changes in the transmitted particle spectrum and LET distribution. The magnitude of the observed transformation remains configuration-dependent. Shield geometry, radiation environment, solar modulation, target material, areal density, and response function can all influence the numerical outcome.

4.6 Engineering Significance

Table 5. Transport-field changes between the unshielded and 100 g cm⁻² aluminum cases.

Metric	0 g cm⁻²	100 g cm⁻²	Change
Total integrated flux (particles cm⁻² day⁻¹)	491.32	1477.58	+200.7%
Photon flux (particles cm⁻² day⁻¹)	315.15	923.30	+193.0%
Proton flux (particles cm⁻² day⁻¹)	9.06	42.80	+372.6%
Ni-58 flux (particles cm⁻² day⁻¹)	1.566	0.00182	−99.88%
Heavy-ion flux, Li–Ni (particles cm⁻² day⁻¹)	1.842	0.097	−94.74%
Flux >10 keV µm⁻¹ (particles cm⁻² day⁻¹)	1.920	0.229	−88.05%
Flux >100 keV µm⁻¹ (particles cm⁻² day⁻¹)	1.696	0.0158	−99.07%
Flux >1000 keV µm⁻¹ (particles cm⁻² day⁻¹)	0.0203	8.33×10^{-5}	−99.59%

From an engineering perspective, the 100 g cm⁻² case greatly suppresses the original high-Z component and the extreme-LET tail but simultaneously generates a larger population of lower-LET secondary particles. Accordingly, attenuation of selected primary components and simplification of the transmitted radiation field are not equivalent concepts.

The transport indicators developed here can be retained unchanged in future material comparisons. A polyethylene or hybrid aluminum–polyethylene OLTARIS simulation using the same BO-20 model, solar condition, Martian-surface environment, geometry, and response functions would allow direct comparison of both dose-related and radiation-field transformation metrics.

4.7 Study Limitations

- The study is computational and does not constitute an experimental measurement.
- The spherical geometry is an idealized configuration and does not reproduce the detailed geometry of an operational spacecraft or habitat.
- Only the recorded GCR environment is analyzed; Solar Particle Events are not included.
- Particle-fraction interpretation is constrained by the recorded nickel-specific OLTARIS configuration.
- The energy-integrated flux metric depends on the exported energy grid and should not be interpreted as a dosimetric quantity.
- REIC and REID numerical values are not reported because the corresponding raw numerical files were not independently verified in the supplied dataset.
- Configuration-specific effective-dose and organ outputs are not assigned to an aluminum-thickness response curve unless a thickness index is explicitly recoverable.

5. Conclusion

This study characterized the transformation of the Martian-surface GCR radiation field through increasing aluminum areal density using NASA OLTARIS/HZETRN. The analysis demonstrates that shielding response cannot be represented adequately by particle attenuation alone.

The total transported particle flux increased from approximately 491.3 to 1477.6 particles cm^{-2} day^{-1} between 0 and 100 g cm^{-2}, while Ni-58 flux decreased by approximately 99.88% and proton flux increased by approximately 372.6%. The heavy-ion contribution to absorbed dose decreased from 96.65% to 8.20% in the recorded configuration, accompanied by increasing contributions from protons, electrons/positrons, pions, and D/T/He particles.

The high-LET tail was strongly suppressed, with cumulative flux reductions of approximately 88.05%, 99.07%, and 99.59% above 10, 100, and 1000 keV μm^{-1}, respectively. These findings show that aluminum changes both the magnitude and composition of the transmitted radiation field through coupled attenuation, fragmentation, and secondary-particle production.

The principal practical implication is that shielding optimization for human deep-space missions should jointly consider particle flux, absorbed dose, radiation quality, and biologically relevant response quantities. The present aluminum dataset provides a traceable transport baseline for future comparisons with polyethylene, Martian regolith, metal hydrides, and hybrid shielding architectures.

5.1 Future Work

- Repeat the Martian-surface BO-20/2010 solar-minimum scenario with the complete GCR particle population rather than a species-specific nickel selection.
- Retain the eleven aluminum areal densities so that future material comparisons remain directly comprable.
- Evaluate polyethylene and at least one hybrid aluminum–polyethylene configuration using identical geometry and response functions.
- Export and preserve complete REIC and REID numerical datasets for future biological-risk analysis.
- Compare total flux, cumulative high-LET flux, absorbed dose, leukemia dose equivalent, and solid-cancer dose equivalent simultaneously across candidate shielding materials.

Data Availability

The numerical analysis was reconstructed from the supplied OLTARIS raw outputs for job_1, including hi_flux_database.dat, hi_Flux_Point_1.dat, hi_mars_surface_bc.dat, hi_dose_frac_database.dat, hi_dose_part_database_mGy.dat, hi_diflet_table.dat, and hi_intlet_table.dat. The datasets contain the multidimensional energy, particle, aluminum-depth, and tissue-depth grids used in the present analysis.

Declarations

Funding: No specific external funding is declared.

Conflict of interest: The authors declare no conflict of interest.

Ethical approval: Not applicable; the study is computational.

Code availability: Radiation transport was performed using NASA OLTARIS/HZETRN; no custom transport code was developed.

Acknowledgements

The authors acknowledge Bayero University, Kano, for the academic environment supporting this research. The authors also acknowledge the use of artificial intelligence (AI)-assisted language and editorial tools during preparation of the manuscript. AI assistance was used to support language refinement, grammatical editing, structural organization, and presentation. The authors remain responsible for the scientific content, numerical data, interpretation of the OLTARIS results, conclusions, and final manuscript.

References

1. Hassler, D. M., Zeitlin, C., Wimmer-Schweingruber, R. F., et al. (2014). Mars' surface radiation environment measured with the Mars Science Laboratory's Curiosity rover. Science, 343(6169), 1244797. https://doi.org/10.1126/science.1244797.
2. Durante, M., & Cucinotta, F. A. (2011). Physical basis of radiation protection in space travel. Reviews of Modern Physics, 83(4), 1245–1281. https://doi.org/10.1103/RevModPhys.83.1245.
3. Simpson, J. A. (1983). Elemental and isotopic composition of the galactic cosmic rays. Annual Review of Nuclear and Particle Science, 33, 323–381.
4. Wilson, J. W., Townsend, L. W., Schimmerling, W., et al. (1995). Transport methods and interactions for space radiations. NASA Technical Publication.
5. Slaba, T. C., Bahadori, A. A., Reddell, B. D., et al. (2017). Optimal shielding thickness for galactic cosmic ray environments. Life Sciences in Space Research, 12, 1–15.
6. Slaba, T. C., & Whitman, K. (2020). The Badhwar–O'Neill 2020 GCR model. Space Weather, 18, e2020SW002456. https://doi.org/10.1029/2020SW002456.
7. Singleterry, R. C., Blattnig, S. R., Clowdsley, M. S., et al. (2011). OLTARIS: On-line tool for the assessment of radiation in space. Acta Astronautica, 68(7–8), 1086–1097. https://doi.org/10.1016/j.actaastro.2010.09.022.
8. Sreedevi, V. V., & Lalwani, K. (2025). Effectiveness of Multi-Layered Radiation Shields Constructed from Polyethylene and Metal Hydrides Using HZETRN and OLTARIS for Space Applications. Journal of Space Science and Technology, 18(Special Issue S1). https://doi.org/10.22034/jsst.2025.1520.

Nomencla]ture

Table 6. Nomenclature used in the manuscript.

Symbol/term	Meaning	Unit
GCR	Galactic Cosmic Rays	—
HZE	High-charge and high-energy ion	—
LET	Linear Energy Transfer	keV μm^{-1}
$\Phi(E)$	Differential particle flux	particles cm^{-2} day^{-1} per energy
F_j	Energy-integrated particle flux	particles cm^{-2} day^{-1}
ρA	Aluminum areal density	g cm^{-2}
D	Absorbed dose	Gy
H	Dose equivalent	Sv